LAWRENCE
LIVERMORE
NATIONAL
LABORATORY

LLNL-JRNL-841998

Crustal Structure of the Mesopotamian Plain, East of Iraq

W. Abdulnaby, K. Motaghi, E. Shabainan, H. Mahdi, H. Al-Shukri, R. Gok

November 2, 2022

Tectonics

Disclaimer

AGU ADVANCING EARTH AND SPACE SCIENCE

Tectonics

RESEARCH ARTICLE
10.1029/2020TC006225

Special Section:
Tethyan Dynamics: From Rifting to Collision

Crustal Structure of the Mesopotamian Plain, East of Iraq

Wathiq Abdulnaby[1], Khalil Motaghi[2], Esmaeil Shabanian[2], Hanan Mahdi[3], Haydar Al-Shukri[3], and Rengin Gök[4]

[1]Seismological Laboratory of University of Basrah (SLUB), Department of Geology, College of Science, University of Basrah, Basrah, Iraq, [2]Department of Earth Sciences, Institute for Advanced Studies in Basic Sciences (IASBS), Zanjan, Iran, [3]University of Arkansas at Little Rock (UALR), Little Rock, AR, USA, [4]Lawrence Livermore National Laboratories (LLNL), Livermore, CA, USA

Abstract The crustal structure of Iraq was investigated through analyzing teleseismic data from 12 new seismic stations. Three seismic stations are located within the Zagros Fold-Thrust Belt, and nine are within the Mesopotamian Plain. Joint inversion of *P* wave receiver function and Rayleigh wave dispersion data were employed to resolve *S* wave velocity structure models beneath each station. Combining these models with available Moho depths within and around the study area reveals that the Moho depth is smoothly increasing from the Arabian platform toward the Zagros Mountains. An exceptional deeper root is observed near the eastern edge of the Mesopotamian Plain where sedimentary pile is the thickest. This root was interpreted as a structure inherited from the successive Mesozoic rifting of the NE Arabian platform enhanced by sedimentary loading and progressive subsidence. A low-velocity uppermost mantle was observed beneath the Arabian Foredeep attesting the existence of a low-strength lithospheric mantle beneath the region southwest from the Zagros deformation front. The weak rheology of the uppermost mantle may have allowed local sinking of the crust and deepening of the Moho boundary due to vertical loading and the Late Miocene lateral contraction.

Key Points:
- We found an abnormal crustal root in SE of the Mesopotamian Plain using receiver function analysis for 12 new seismic stations in Iraq
- The crustal root is a structure inherited from the Mesozoic rifting of the NE Arabian platform during Triassic and Middle to Late Jurassic
- Low-velocity uppermost mantle beneath the Mesopotamian Plain allowed local sinking of the crust and deepening of the Moho boundary

Correspondence to:
K. Motaghi,
khalil1024@yahoo.com

Citation:
Abdulnaby, W., Motaghi, K., Shabanian, E., Mahdi, H., Al-Shukri, H., & Gök, R. (2020). Crustal structure of the Mesopotamian Plain, east of Iraq. *Tectonics*, *39*, e2020TC006225. https://doi.org/10.1029/2020TC006225

Received 4 APR 2020
Accepted 15 OCT 2020
Accepted article online 19 OCT 2020

1. Introduction

Internal structures and geophysical characteristics of the continental crust differ according to distinct tectonic histories experienced by the continent. The crustal characteristics, in turn, control rheological responses of the continental crust to ongoing tectonic deformations and vertical loading that are principal factors in continental deformation and the evolution of young mountain belts. Knowledge of the deep structure of the crust and the uppermost mantle is, thus, crucial for the better understanding of (1) the response to elastic flexure of the lithosphere since it is loaded by the topographic wedge and sediment accumulation during mountain building, and (2) seismotectonic behavior of the crust in active mountain belts. Such knowledge helps in constraining paleotectonic and geodynamic reconstructions of mountain building processes. The Zagros system is the expression of a young collisional orogeny in which different shallow and deep processes of continental deformation and mountain building are active (e.g., Hatzfeld & Molnar, 2010). During the recent century, several geophysical and geological studies tried to illuminate different aspects of continental deformation in the Zagros orogenic belt (e.g., Austermann & Iaffaldano, 2013; Motaghi et al., 2015; Paul et al., 2006, 2010; Pirouz, Avouac, Gualandi, et al., 2017; Rahmani et al., 2019; Snyder & Barazangi, 1986). Almost all of these past studies focused on the Iranian part of the Zagros, mostly due to the lack of data/research on the southwest part of the orogen (the Mesopotamian foreland and its SW margin). This always has led to a classic simplification of the crustal structure of the Arabian platform southwest from the Zagros deformation front, which approximates the political boundary of Iran in the southwest and west of Zagros.

This paper is investigating the lithospheric structure of the northeastern part of the Arabian plate, mostly including the Mesopotamian Plain, which is the onshore part of the Zagros Mountains Foredeep in eastern Iraq. The northeast margin of the Arabian plate collided with Central Iran at ~27 Ma (e.g., Egan et al., 2009; McQuarrie & van Hinsbergen, 2013; Pirouz, Avouac, Hassanzadeh, et al., 2017) followed by the Arabia-Eurasia convergence, with a rate of <17 mm/yr in the northwest increasing to <24 mm/yr in the southeast (e.g., Khorrami et al., 2019). The Zagros Mountains accommodated a third of the present-day total convergence. The across-belt convergence is accommodated through different mechanisms of diffused

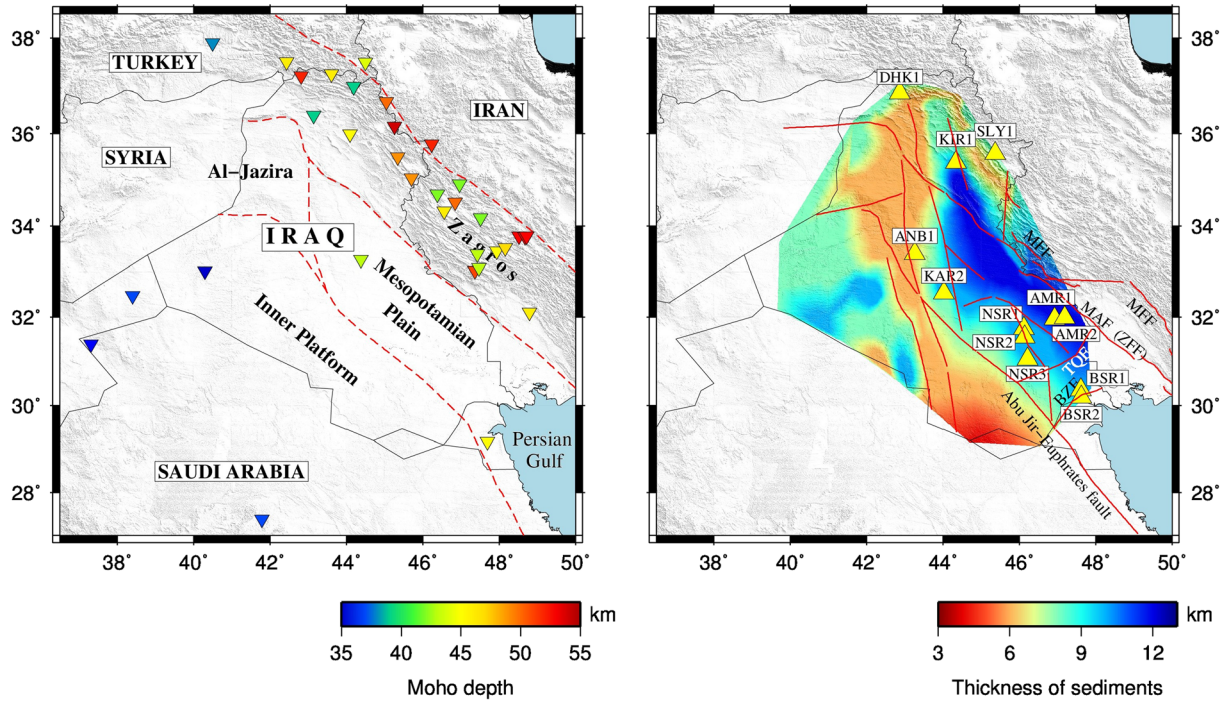

Figure 1. Shaded relief (GTOPO30) of the study area. (left) Tectonic division of Iraq (dashed lines) from Fouad (2010a, 2010b) and Sissakian et al. (2017). Black line is the border of countries. Moho depth from previous studies (Table 1) is reported for 33 seismic stations. (right) Seismic stations used in this study are marked by yellow triangles. The thickness of the sedimentary layer is replotted from Jassim and Goff (2006: Figure 4–6). Red lines mark the location of basement faults in Iraq based on Berberian (1995), Mohammed (2006), Fouad (2015), Sissakian et al. (2017), and Abdulnaby (2019). MAF, Makhul-Amara fault; ZFF, Zagros Foredeep Fault; TQF, Takhadid-Qurna Fault; BZF, Basrah-Zubair Fault; MFF, Mountain Front Fault.

shortening such as folding, decoupling, and thickening at the lithospheric scale resulting in internal deformation of the Arabian plate margin (e.g., Motaghi, Shabanian, Tatar, et al., 2017; Priestley et al., 2012) and/or underthrusting of the Arabian lithosphere beneath Central Iran (e.g., Motaghi, Shabanian, & Kalvandi, 2017; Paul et al., 2010).

Iraq comprises two main tectonic provinces (e.g., Fouad, 2015; Sissakian et al., 2017): (1) the tectonically unstable Outer Platform consisting of the NW Zagros Fold-Thrust Belt and the Mesopotamian Foredeep; (2) the stable Inner Platform that covers the western desert of Iraq. The Mesopotamian Foredeep consists of Al-Jazira and the Mesopotamian Plain (Figure 1). The Mesopotamian Plain is the present-day expression of a long-lasting sedimentary trough at the northeast margin of the Arabian platform. The sedimentary cover in the Mesopotamian Plain ranges from 7 km in the southwest (e.g., near KAR2 in Figure 1) to 14 km in the northeast (e.g., near BSR1–2 in Figure 1) (Al-Ameri, 2011; Jassim & Goff, 2006; Mohammed, 2006; Figure 1). At its southwestern boundary, the Mesopotamian Plain is bordered by the Abu Jir-Euphrates fault against the Inner Platform such that the fault separates the relatively thick (7–14 km) sedimentary cover of the Mesopotamian Plain from a thin (~2–4 km) sedimentary cover in western Iraq (Jassim & Goff, 2006; Mohammed, 2006). The Abu Jir-Euphrates fault is clearly observed as basement fault steps in seismic lines (Mohammed, 2006) and bounds the southwest margin of the Triassic and Middle to Late Jurassic rift systems (e.g., Fadhel & Al-Rahim, 2019). Deep-seated normal faults such as the Abu Jir-Euphrates fault were inherited from the extension of northeast passive margin of the Arabian plate during the Triassic time (Numan, 1997, 2000). The Middle to Late Jurassic rift system superimposed this initial rift system and its sedimentary sequences, reactivating the preexisting graben and horst structures in the Mesopotamian Plain (see Fadhel & Al-Rahim, 2019 for more details). Since Late Jurassic, subsidence across the graben system faults has continued in the area, and an almost continuous sedimentary succession formed in this tectonic depression (Jassim & Goff, 2006). In Middle Cretaceous, the Arabian plate transitioned from extensional to compressional tectonics leading to reverse reactivation of preexisting normal faults and marginal folding (see Aqrawi et al., 2010; Fadhel & Al-Rahim, 2019;

Numan, 1997, 2000). This tectonic inversion, however, has locally affected the basin and produced short-wavelength fault-related anticlines close to the inverted graben bounding faults (e.g., Darweesh et al., 2017; Fadhel & Al-Rahim, 2019). According to the burial thermal histories of the Middle Jurassic–Early Cretaceous source rocks in the Mesopotamian Plain, the uniform subsidence of the basin was followed by rapid subsidence at 15–10 Ma during which a ~3-km-thick sedimentary pile of Upper Miocene-Pliocene deposits accumulated in the fault-bounded depocenters (Aqrawi & Badics, 2015).

Except for the Abu Jir-Euphrates boundary fault, other crustal faults do not emerge at the surface in the Mesopotamian Plain and are covered by Cenozoic sedimentary layers. For this reason, there is no consensus on the location, geometry, and extent of some longitudinal and transverse faults of the Mesopotamian Plain (compare Abdulnaby, 2019; Fouad, 2015; Sissakian et al., 2018). In this study, a fault map was compiled (Figure 1) including the most accepted basement fault trends supposed/documented through the analysis of magnetic/gravity data, seismic lines, and oil wells data (Abdulnaby, 2019; Fouad, 2015; Jassim & Goff, 2006; Sissakian et al., 2014, 2017). Based on available geological and geophysical information (Fouad, 2015; Jassim & Goff, 2006), the Mesopotamian Foredeep comprises three distinct northwest, central, and southeast structural domains with different structural patterns and styles of deformation (e.g., Fouad, 2015). The northwest domain includes subsurface NW trending narrow graben structures. The central domain hosts the NW-SE Triassic and Middle to Late Jurassic horst and graben structures accompanied by subsurface NW trending fault-related anticlines. The southeast domain is the only part affected by Hormuz basal salt movements and the N-S structures inherited from the Arabian plate breakout. Basement transverse faults (e.g., Basrah-Zubair and Takhadid-Qurna faults; Figure 1) control the boundary of these structural domains (e.g., Jaffar & Abdulnaby, 2018), while the longitudinal faults (e.g., Abu Jir-Euphrates and Makhul-Amara faults; Figure 1) define stepping boundaries of Jurassic-Pliocene sedimentary basins. The NE dipping Zagros Foredeep Fault (ZFF; Berberian, 1995) follows the subsurface trend of the Makhul-Amara basement fault.

There is no detailed study on the crustal structure of Iraq. Most of the reported crustal thicknesses are from the NE corner of Iraq where the Zagros orogen enters the country (Figure 1). The depth of Moho below the seismic stations studied in the NW Zagros and the Mesopotamian Plain are summarized in Table 1 and Figure 1. Sparse reports for Moho depth (Gök et al., 2008; Pirouz, Avouac, Gualandi, et al., 2017) depict that the crust is thin (thickness ~35 km) and unreformed beneath the Inner Platform, while it is thicker (>40 km) and shortened beneath the Zagros Mountains. Pirouz, Avouac, Hassanzadeh, et al. (2017) assumed a smooth increase in the Moho depth from the Inner Platform side to the Zagros Mountains due to elastic bending of the lithosphere under vertical loads in the front of the Zagros collision. The only report for the Moho depth in the Mesopotamian Plain comes from Baghdad station (~43 km, Gök et al., 2008) consistent with an eastward dipping Moho boundary.

This paper presents the crustal structure for 12 sites in Iraq, nine of which are located within the Mesopotamian Plain. The teleseismic data were used to obtain 1-D *S* velocity structure beneath each station using joint inversion of *P* receiver function and Rayleigh wave dispersion (Julia et al., 2000). For each station, one high-quality stacked receiver function was calculated and jointly inverted with fundamental mode Rayleigh wave group velocity extracted from an ambient noise tomography for the Middle East (Kaviani et al., 2020). The resulting models reveal unexpected crustal thickness variations beneath the Mesopotamian Plain. This sheds more light on the crustal structure of the northeastern part of the Arabian plate and the tectonic evolution of the Zagros collision.

2. Data Preparation

As part of network improvement project in the Middle East, Lawrence Livermore National Laboratory (LLNL) of the U.S. Department of Energy funded the installation of broadband and strong-motion stations in Iraq. The deployment has started in May 2014 in collaboration with University of Basrah, University of Summar, University of Sulaymaniyah, and University of Duhok to install a regional network in eastern Iraq, mostly in the Mesopotamian Plain, in collaboration with University of Arkansas at Little Rock (UALR). Seismic station names, coordinates, and operating dates are presented in Table 2. Stations DHK1, KIR1, and SLY1 are located at the edge of the Zagros Mountains, while the others are located inside the Mesopotamian Plain. The instruments are three-component Güralp Systems (CMG-40T and

Table 1
Crustal Thickness (Moho Depth) of the Northeastern Margin of the Arabian Plate in Iraq and Surrounding Regions

Country	Station name	Latitude	Longitude	Moho depth (km)	Reference
Jordan	RUWJ	32.4750	38.4020	37	Al-Damegh et al. (2005)
Saudi Arabia	HILS	27.3800	41.7900	37	
	QURS	31.3900	37.3200	33	
Kuwait	KBD	29.1755	47.6933	45	Pasyanos et al. (2007)
Iran	DHR	34.6997	46.3860	42	Afsari et al. (2011)
	GHG	34.3294	46.5686	46	
	KOM	34.1764	47.5144	42	
	LIN	34.9186	46.9624	42	
	VIS	34.5253	46.8527	50	
	E1	33.091	47.4788	43	Motaghi, Shabanian, and Kalvandi (2017)
	E2	33.3952	47.4319	43	
	V6	33.4507	47.9391	45	
	E3	33.5261	48.1602	47	
	V10	33.0254	47.3704	51	
	V4	33.7843	48.5217	59	
	V1	33.7833	48.7209	60	
	SHGR	32.108 46	48.801	46	Tatar and Nasrabadi (2013)
Turkey	CUKT	37.2473	43.6077	46	Mellors et al. (2008)
	SEMD	37.5000	44.5000	44	
	SIRT	37.5010	42.4392	46	
	MRDN	37.9000	40.5000	38	Gök et al. (2007)
Iraq	KSBB	35.0415	45.7092	49	Gritto et al. (2008)
	KSSS	35.7696	46.2362	52	
	KSWW	36.1493	45.2624	54	
	KSJS	35.4965	45.3452	49	
	KEHH	36.6764	45.0470	50	
	KESM	36.9846	44.1981	39	
	KDDA	37.2125	42.8207	52	
	KEKZ	35.9893	44.0970	45	
	MSL	36.3817	43.1483	39	Gök et al. (2008)
	BHD	33.2700	44.3800	43	
	RTB	33.0200	40.3000	35	Al-Heety (2002)
	DHK	36.8606	42.8665	40	Abdulnaby (2013)

Table 2
Locations of the Seismic Stations Along With Duration of Data Collections Used in This Study

Station code	Latitude	Longitude	Begin YYYY/MM/DD	End YYYY/MM/DD	Sediment thickness	Crustal thickness	Analyzed waveforms	No. of RFs
AMR1	31.9590	46.9286	2015/03/06	2015/10/31	16 km	50 km	219	27
AMR2	31.9899	47.1902	2015/11/07	—	16 km	52 km	878	62
ANB1	33.401	43.2576	2019/11/01	—	—	47 km	271	94
BSR1	30.3581	47.6153	2014/08/10	2015/08/28	17 km	47 km	318	68
BSR2	30.2927	47.6191	2015/08/18	—	17 km	48 km	1,041	102
DHK1	36.8606	42.8665	2007/10/03	—	4 km	43 km	721	102
KAR2	32.5398	44.0224	2017/01/15	—	11 km	44 km	510	102
KIR1	35.388	44.3419	2018/11/01	—	—	48 km	246	55
NSR1	31.7416	46.1151	2014/05/29	2017/10/07	14 km	48 km	627	26
NSR2	31.5550	46.1374	2014/05/29	2014/09/21	14 km	46 km	26	9
NSR3	31.0514	46.2199	2014/05/28	2014/11/30	14 km	44 km	94	21
SLY1	35.5784	45.3667	2015/09/15	—	—	47 km	1,194	145

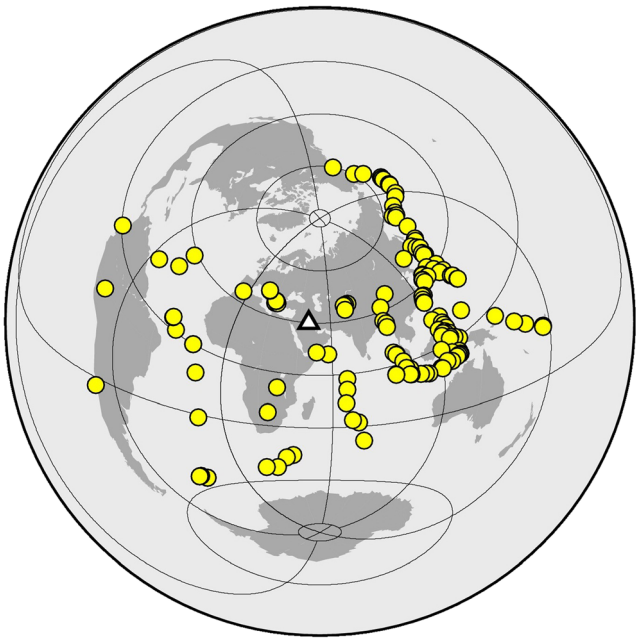

Figure 2. Azimuthal distribution of teleseismic events (circles) used in this study in relation to the study area (triangle).

CMG-3ESP) with 24-bit digitizers (CMG-DM24) and with GPS timing system. The stations were repositioned during the deployment, and the recording span at individual stations varied between 4 months and 2 years (Table 1).

Two data sets were prepared to conduct *S* velocity modeling for each seismic station. Among the teleseismic waveforms recorded by the stations, we selected teleseismic events with an epicentral distance between 25° and 140° and magnitude greater than 5.4 (Figure 2). For each waveform, the theoretical P/P_{diff} onset was calculated using the IASP91 standard velocity model (Kennett & Engdahl, 1991). The onset was then used to extract the teleseismic *P* window started from 50 s before and 100 s after the time. The three-component waveforms were band-pass filtered between 0.05 and 2 Hz and rotated from ZNE into ZRT coordinate system. Using the iterative deconvolution method of Ligorria and Ammon (1999), the *Z* component was deconvolved from *R* and *T* components, and a Gaussian filter with a Gaussian width of 3.0 was applied to each receiver function. A moveout correction (to ray parameter = 0.06 s/km) was then made using standard velocity model of the IASP91, and the individual receiver functions were then stacked. Thus, one high-quality stacked receiver function was presented for each station. Figures 3 and 4 show these stacked and individual moveout corrected receiver functions. Dispersion data for Rayleigh wave group velocity come from the ambient noise tomography of Kaviani et al. (2020). The group velocities were measured for the region in the period range of 5–100 s. The group velocity maps were interpolated to obtain a site-specific dispersion curve.

3. Inversion Procedure

A brief description is provided below of the procedure used for joint inversion of stacked receiver function and surface wave dispersion. The procedure was described with more details by Motaghi et al. (2015), Motaghi, Shabanian, and Kalvandi (2017), and Rastgoo et al. (2018). The program *joint96* was employed to invert data to *S* velocity model. The program is available in the software package "Computer Programs in Seismology" (Herrmann, 2013).

A search for "optimal" parameterization was carried out following the stability test presented by Motaghi et al. (2015). In this test, the Incremental Step (IS) was considered in the nonlinear inversion of dispersion data (taken from Rahimi et al., 2014) as the thickness of layers in the initial velocity model. The IS is the minimum layer thickness resolvable due to inversion of dispersion data. The high-frequency receiver function (with Gaussian width of 3) is sensitive to smaller features in comparison with dispersion data. Thus, the layers of the initial velocity models are divided into sublayers with thickness equal to IS divided by 1.0, 1.25, 1.50, and 2.0. The inversion was carried out for each parameterization, and percentage of fit to observed receiver function was checked. If a subdividing layer thickness was improving the fitness to the receiver function, the new parameterization was accepted. Otherwise, the coarser model was considered as the optimum parameterization to avoid fine-scale features that are not supported by the data.

Two important factors in joint inversion procedure are *P* and damping. Factor *P* is the contribution percentage of the dispersion data in comparison with receiver function. In the formulation of Julia et al. (2000), the weighting functions for receiver functions and dispersion data are related to $(1 - P)$ and *P*, respectively. $P = 0.15$ (=85% dependency on receiver functions) was chosen to weight more to receiver functions and resolve smaller scale features required for a high-resolution model for the region of study. For three stations, we found that the fitness to dispersion data is not good enough (<99.9%), so we changed the *P* value to 0.2 (for KIR1 and SLY1) and 0.25 (for DHK1) to improve the fitness. The damping factor was fixed to 0.4, which is experimentally the minimum acceptable value. Following Motaghi, Shabanian, and Kalvandi (2017), attempts were made to remove the small-scale features resolved due to the selection of an improper damping factor or *P* by simplifying the final model as was described below. This successfully removes the fine-scale features in the model not supported by the data.

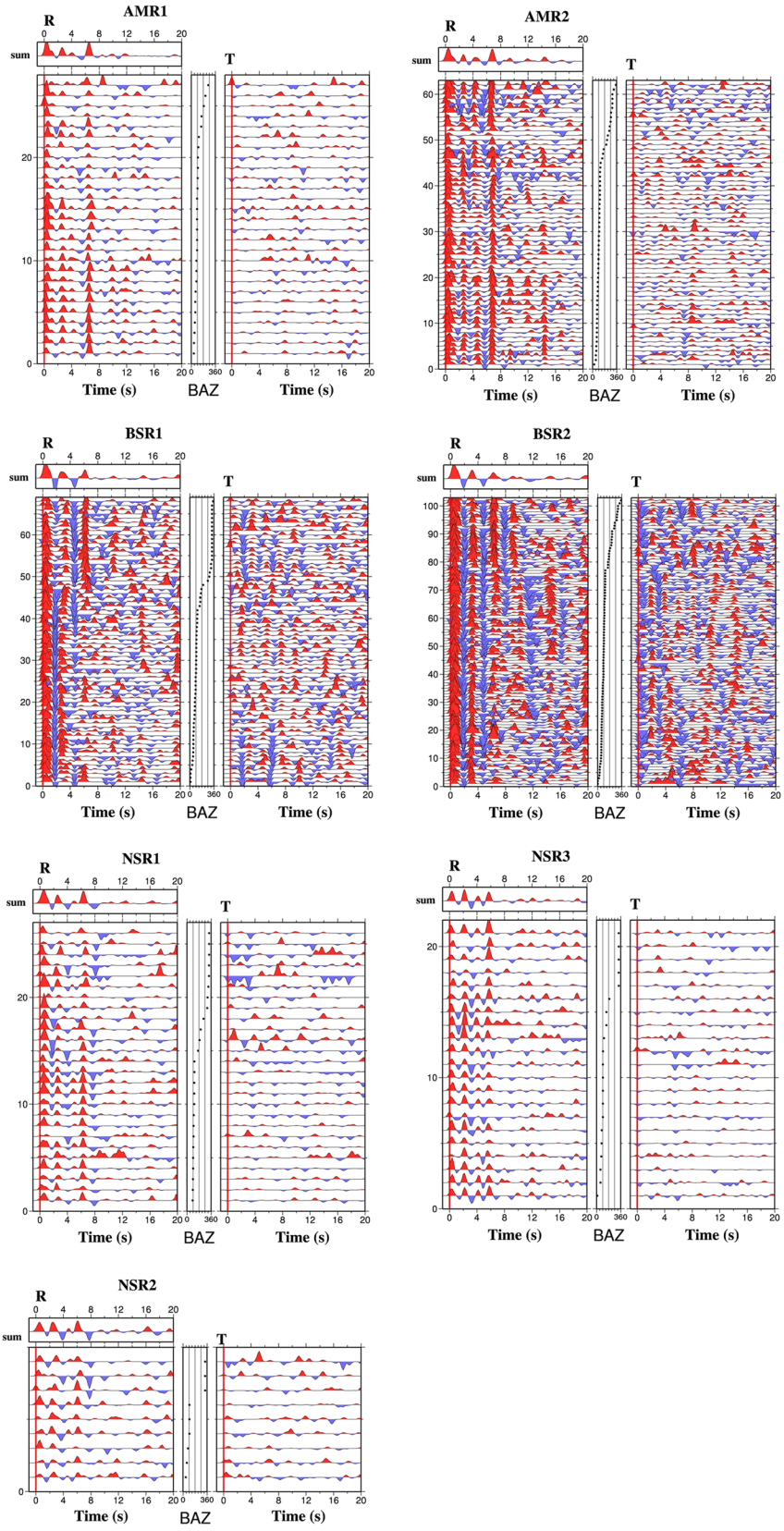

Figure 3. The stacked and individual moveout corrected receiver functions for stations located in south of Iraq. The traces are arranged with increasing theoretical back azimuth shown with black dots.

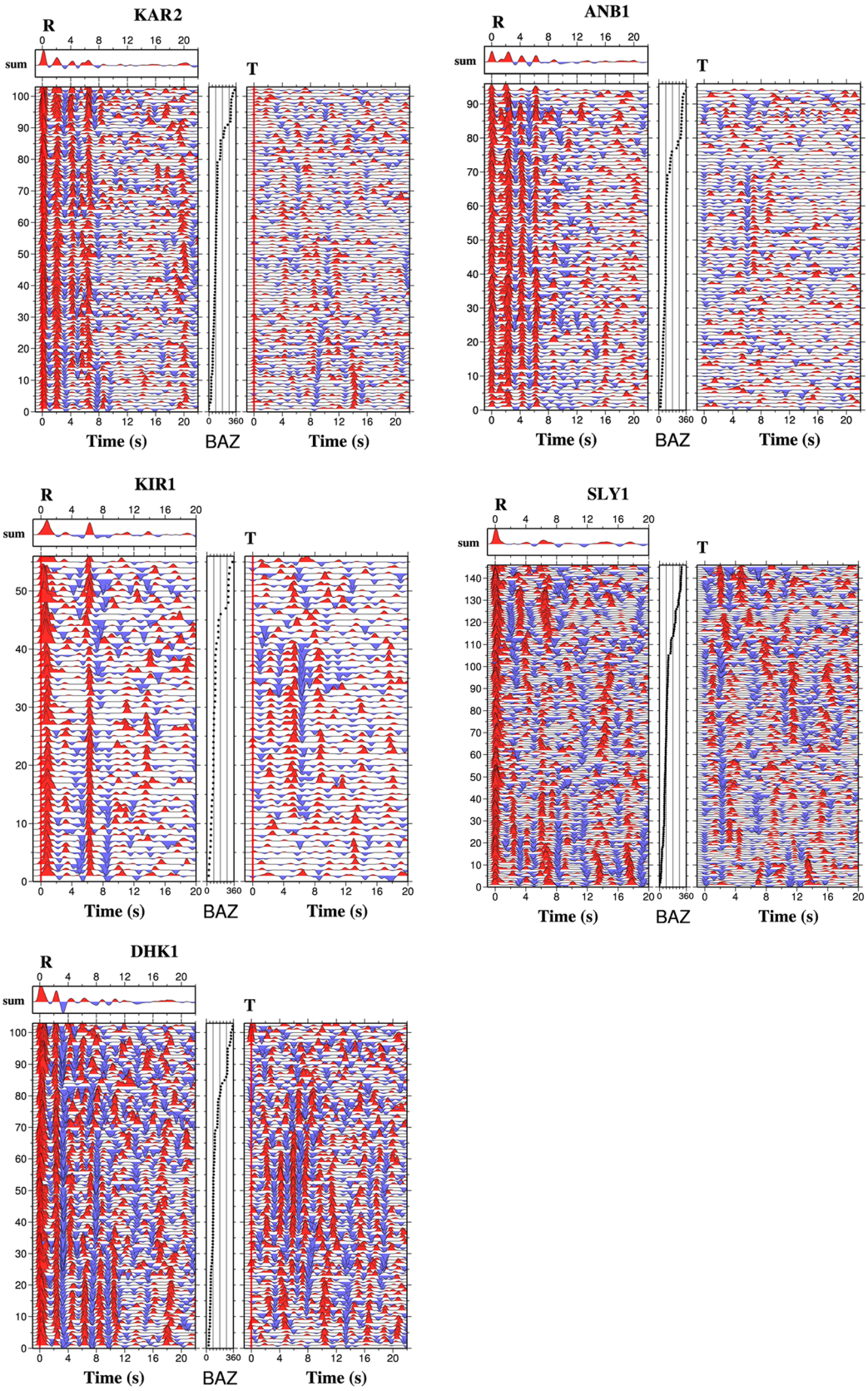

Figure 4. Same as Figure 3 for stations located in middle and north of Iraq.

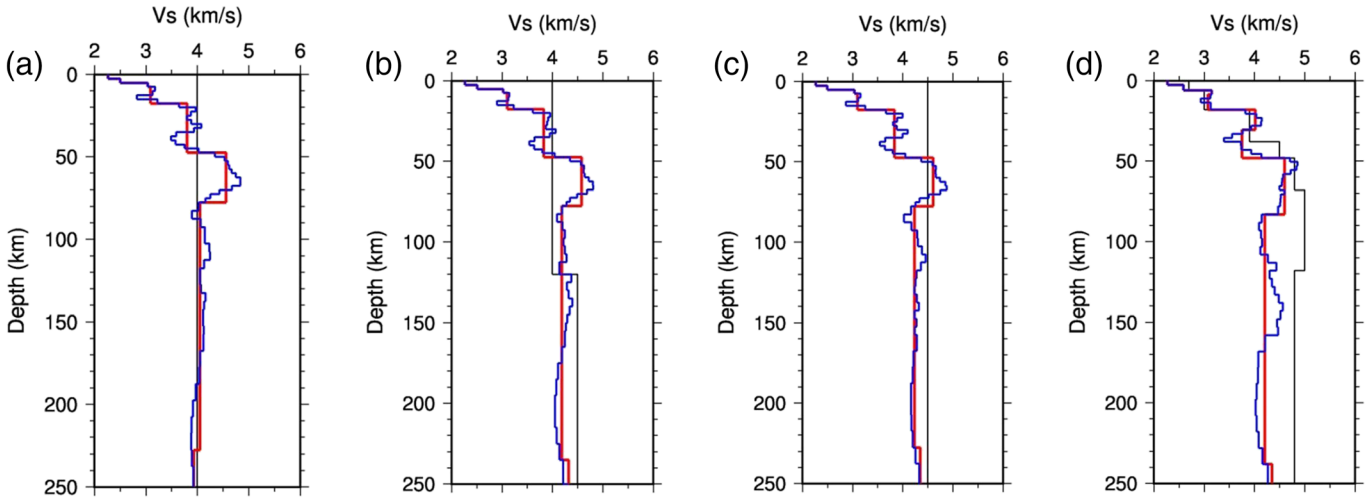

Figure 5. The result of joint inversion of receiver function and dispersion data for BSR1 station. Each subpanel shows output model (blue line) obtained with a different initial velocity model (black line). Similarity of simplified output models (red lines) confirms insignificant sensitivity of inversion on the initial models.

The iterative joint inversion is controlled by a misfit function between the theoretical and observed receiver functions. The inversion is terminated; either the misfit variation in the successive iteration is less than 0.05%, or the maximum number of iterations exceeds 50.

A half-space initial velocity model (Vs = 4.0 km/s) was used for the joint inversion procedure. The joint inversion of the receiver function and dispersion data is weakly sensitive to the initial models, and a half-space is good enough for the inversion (e.g., Acton et al., 2011; Julia et al., 2000). To show this independency, we used four different initial velocity models for BSR1 station to carry out the inversion (Figure 5). The models are (1) a 4.0 km/s half-space, (2) a 4.5 km/s half-space, (3) a two-layered model composed of layers with velocity of 4.0 and 4.5 km/s above and below a 120-km-depth interface, and (4) a velocity model belonging to the Zagros Mountains taken from Motaghi, Shabanian, and Kalvandi (2017). The last model is considered in the test to show that even if we use an improper initial model (with anomalous high-velocity uppermost mantle), the output model will not change considerably. Figure 5 shows that the output models (blue lines) and the simplified models (red lines) are very similar to each other. All simplified models show a 48 $\pm$ 1 km Moho depth and an average uppermost mantle velocity of 4.1 $\pm$ 0.1 km/s confirming that half-space initial model is a proper selection for the inversion.

The output models are simplified to avoid small artifacts generated by the inversion. The output velocity model was simplified to one with a smaller number of layers. The main velocity contrasts were identified in the model and then the velocity was averaged between those selected boundaries. Synthetic receiver function and dispersion data have been calculated using the simplified model and were compared with the observed ones. The simplified model was accepted as final if the synthetic data are within the experimental error bar. Otherwise, more fine-scale features (smoothed before) were added to the simplified model in order to find a better fit to the observed data. This is an effective approach to keep robust, reliable velocity features in the models removing fine-scale features not supported by the data.

Figures 6 and 7 show the result of joint inversion of stacked receiver function (black line Figures 6a and 7a) and locally extracted dispersion data (black line in Figures 6b and 7b). Blue lines in Figures 6c and 7c show the output velocity model. The simplified model and its associated synthetic data are shown by red solid lines. Black dashed lines show initial velocity models in Figures 6c and 7c.

4. Results

Figures 3 and 4 show radial and transverse components of the receiver functions for 12 seismic stations located in the north, east, and central part of Iraq. The calculated receiver functions show that embedded layers are flat and isotropic beneath most of the stations in the Mesopotamian Plain (i.e., AMR1, AMR2, NSR1, NSR2, NSR3, and KAR2) because amplitude of transverse components is weak

10.1029/2020TC006225

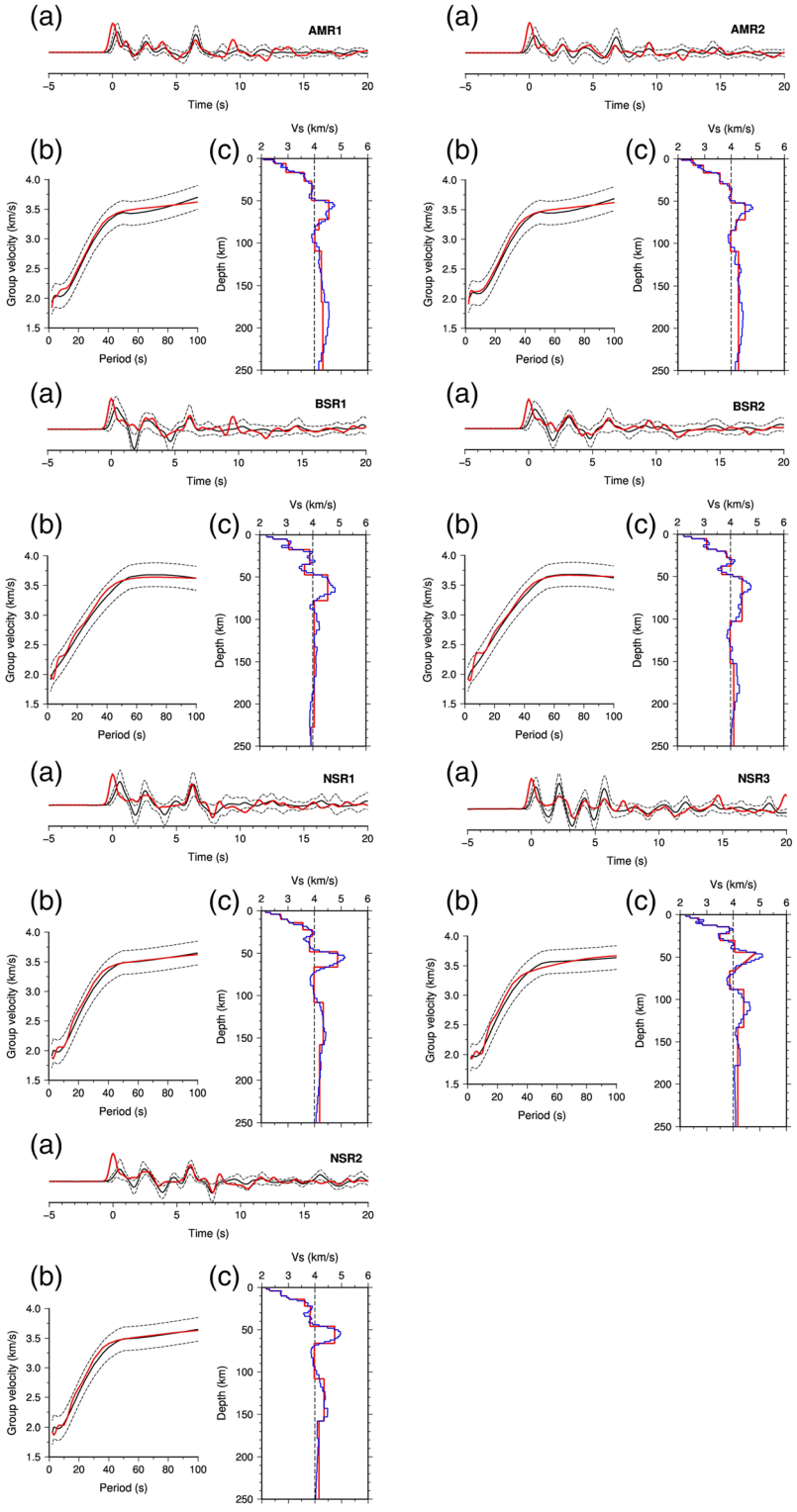

Figure 6. The result of joint inversion of receiver function (RF) and group velocity dispersion data. The name of each station is written on the top right corner of each panel. For each panel, there are three subpanels described here; (a) observed stacked RF (black line) with its error bar (black dashed lines) and synthetic (red line) RF computed for the simplified velocity model shown by the red line in (c). (b) The observed group velocity (solid black line) with its error bar (black dashed lines) and synthetic group velocity (red line) computed for the simplified velocity model shown by the red line in (c). (c) Velocity model obtained from joint inversion (solid blue line) and the simplified model (solid red line), which is considered as the final model. The dashed line is the initial velocity model.

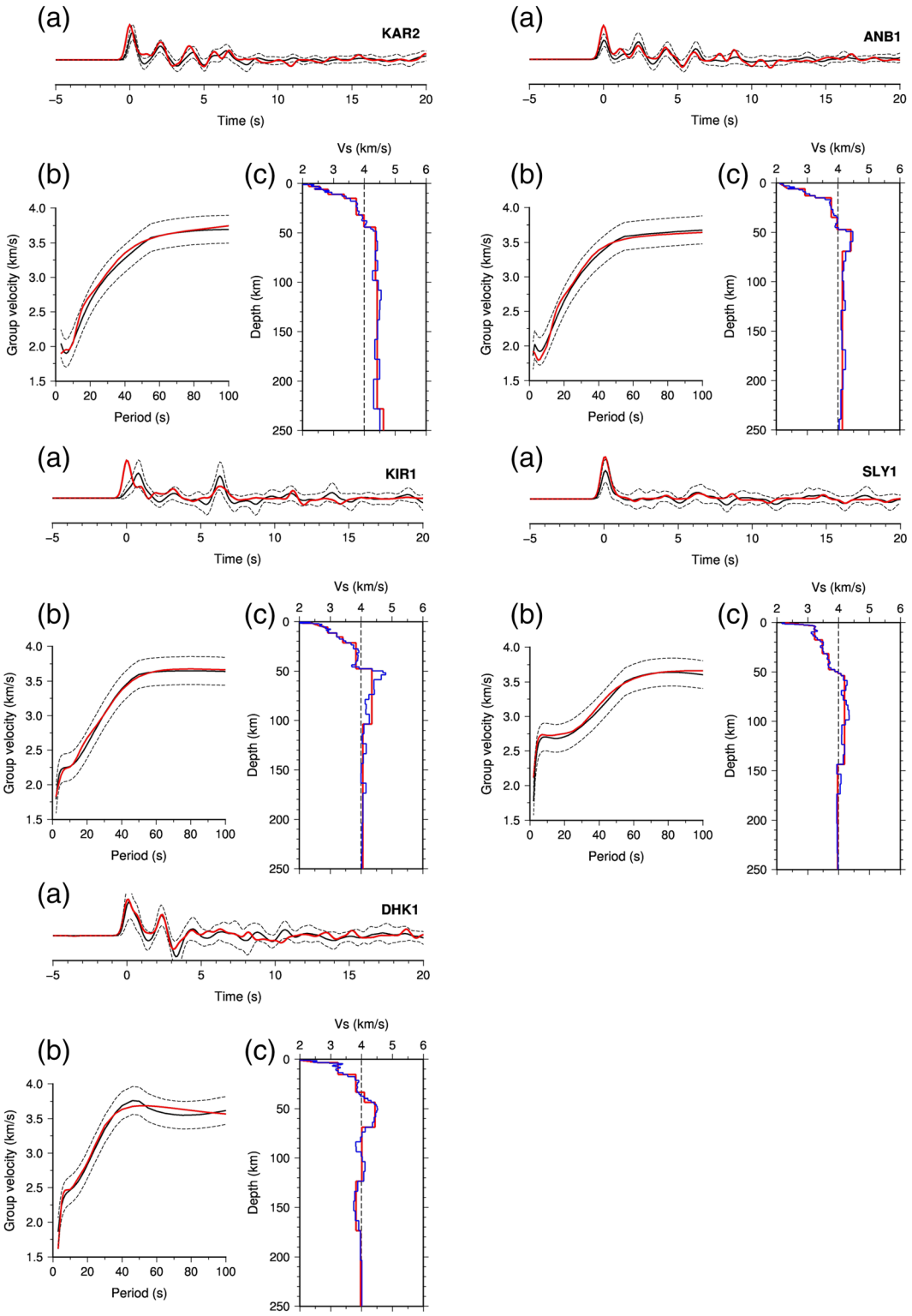

Figure 7. Same as Figure 6 for stations located in middle and north of Iraq.

(e.g., Schulte-Pelkum & Mahan, 2014). Other stations (i.e., BSR1, BSR2, DHK1, KIR1, ANB1, and SLY1) show strong transverse amplitude attesting the existence of dipping and/or anisotropic layers. DHK1, KIR1, and SLY1 are located at the edge of the Zagros Mountains, while BSR1 and BSR2 are located at the southeastern edge of the Mesopotamian Plain (Figure 1).

10.1029/2020TC006225

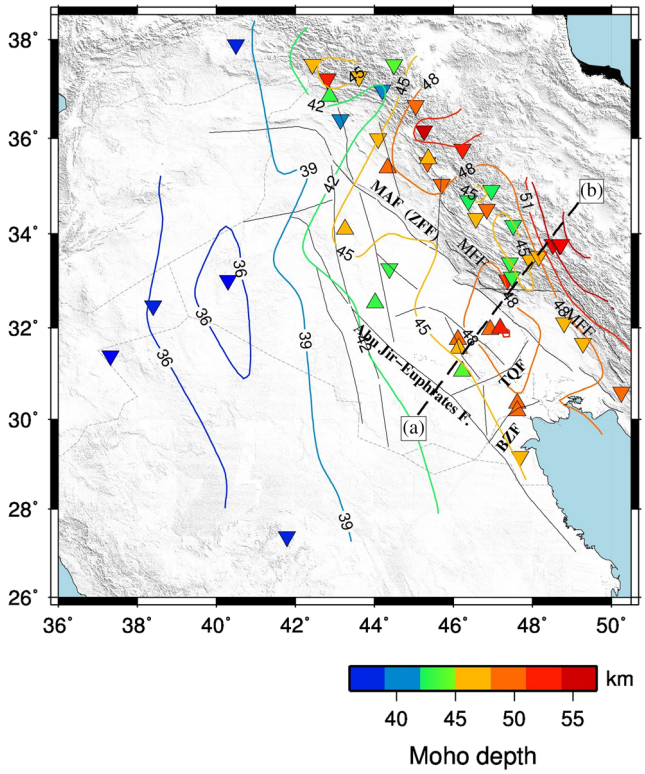

Figure 8. Moho map for Iraq obtained by combining Moho depth beneath previous (inverted triangles) and new (triangles) stations. Line A-B marks the location of the cross section shown in Figure 9. The gray dashed line is the border of countries. Black lines show the location of basement faults in Iraq.

All stations located within the Mesopotamian Plain (i.e., NSR1–3, BSR1–2, AMR1–2, KIR1, and KAR2) show a very clear "delayed *P* wave" where the strong first arrival on the receiver function is well after 0 s, and it has low amplitude. This is often the result of complex shallow structure exists in the foredeep. It is difficult to model the delayed *P* wave arrival with a flat and isotropic 1-D modeling, and this lack of fit (between 0 and 1 s, Figure 6) should be handled by new methods (e.g., Cunningham & Lekic, 2019) which are beyond the scope of this paper.

Crustal thickness beneath the stations located in the study region is variable (Figure 8). The thinnest crust is observed beneath DHK1 (~43 km, Table 2) located at the north of Iraq and inside the folded Zagros. This crustal thickness is consistent with the depth value of ~40 km estimated by Abdulnaby (2013) through the H-k stacking method (Zhu & Kanamori, 2000). The Moho depth is ~44 km beneath KAR2 at the western edge of the Mesopotamian Plain. It increases to ~48 km beneath NSR1, BSR1, and BSR2 reaching the depth of ~52 km beneath AMR2 at the eastern part of the plain (Figures 6–8, Table 2). Taking the location of these stations into account, the overall thickening of the crust toward northeast follows the assumption of flexural bending of the Zagros foreland lithosphere (i.e., the Mesopotamian Plain) due to vertical loading by the Zagros Mountains (Pirouz, Avouac, Gualandi, et al., 2017). A uniform crustal thickening, as predicted by the model, implies that the Moho boundary at the northeast edge of the Mesopotamian Plain (northeast from AMR1 and AMR2) should lie below the depth of 52 km. Nevertheless, shallower Moho depths of ~45 and ~48 km were observed beneath the stations in the northeastern part of Profile A-B (in Figure 8; Afsari et al., 2011; Motaghi, Shabanian, & Kalvandi, 2017). These and other available Moho depths for the Zagros Mountains (ranging from 40 to 50 km below the surface; Motaghi et al., 2015; Paul et al., 2006, 2010; Pirouz, Avouac, Gualandi, et al., 2017; Teknik et al., 2019) do not confirm this overall thickening gradient. Thus, we conclude that the velocity model reveals a local short-wavelength crustal root beneath the Mesopotamian Foredeep, which at the front of the Zagros Mountains is anomalously deeper than nearby areas (Figures 8 and 9).

At shallower depths, we observed various other layers within the upper crust. For instance, a Ps delay time of ~2 s at KAR2 radial receiver functions has been modeled by a velocity boundary at the depth of 11 km (Figure 7). Two converted Ps phases was observed around 1 and 2.5 s at stacked radial receiver functions (Figure 6a) for stations located in the southeastern part of the Mesopotamian Plain (i.e., AMR1, AMR2, BSR1, and BSR2). The inverted velocity models (Figure 6c) show that these pulses are responsible for two velocity boundaries at ~5–7 and ~16–17 km depths (Table 2). The deeper observed interface (in the range of 16–17 km) is close to the boundary between the sedimentary cover and crystalline basement. A maximum depth of 14 km was expected for the sedimentary cover in the Mesopotamian Foredeep based on modeling of Bouguer gravity data (Jassim & Goff, 2006: Figure 4–6; illustrated in Figure 1). The thickness of the crystalline crust (that is, not counting the overlying sedimentary strata) is 30–36 km beneath the Mesopotamian Plain. This is in the range of crystalline crust in the Arabian platform (Gök et al., 2008) and attests slight crustal shortening (e.g., tectonic inversion of rift system faults and internal deformation in the lower crust) under the Zagros Foredeep.

The 1-D velocity models (Figures 6 and 7) reveal a low-velocity (Vs ~ 4.0 km/s) uppermost mantle beneath the Zagros Foredeep. This anomaly was not generated by Vs = 4.0 km/s half-space which was considered as the initial model (dashed lines in Figures 6c and 7c). We note that testing different initial velocity models (Figure 5) has already confirmed that the output models are not dependent on the initial models, and the low-velocity uppermost mantle is obtained even if the velocity of the uppermost mantle in the initial model is assumed ~5.0 km/s (Figure 5d). This low velocity was definitely generated by ~3.6 km/s group velocity at periods >40 s (Figures 6 and 7). This feature will be discussed in the next section.

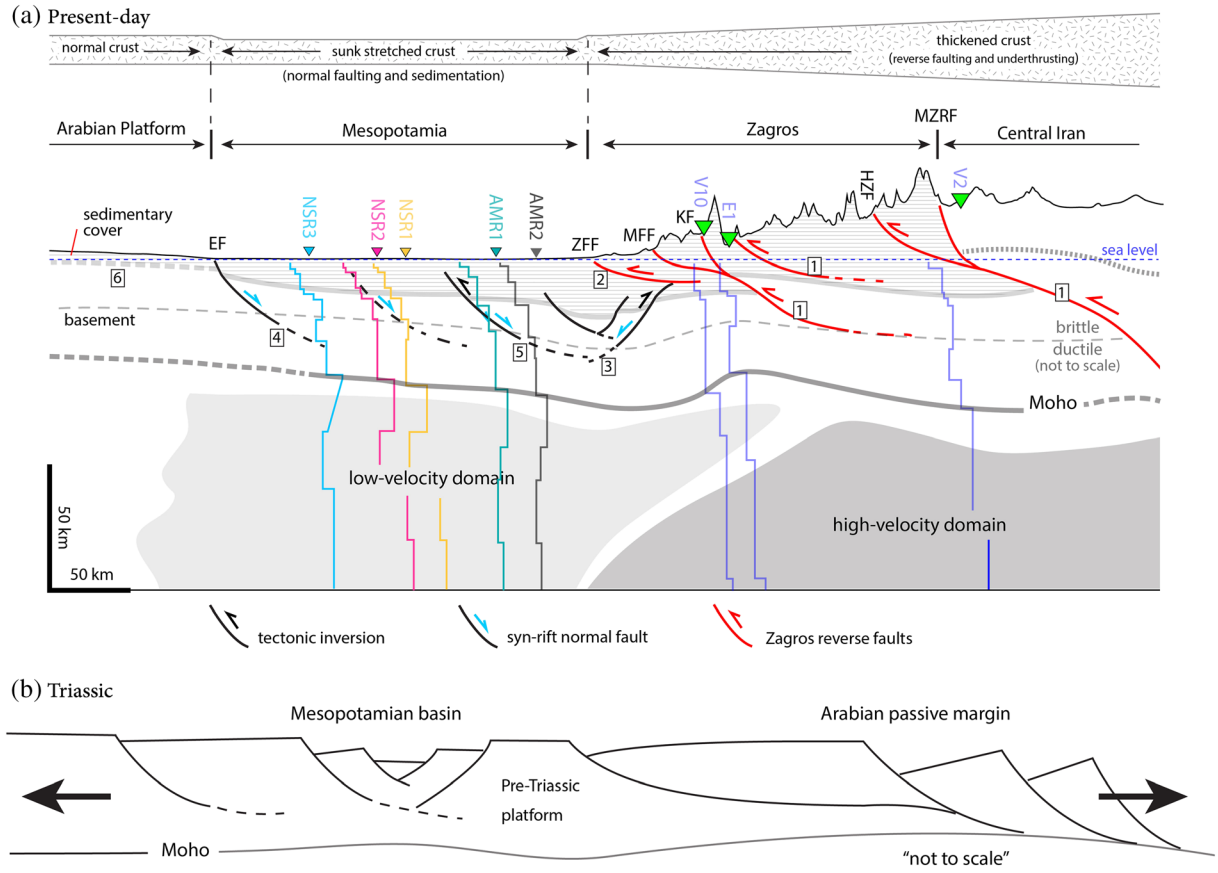

Figure 9. The conceptual tectonic cross section across the Mesopotamian basin illustrating an interpretive summary of our observations. (a) The present-day state of the Arabian platform. The extent of the model and Moho topography is the same as the Profile A-B in Figure 8. Stations (triangles) and the corresponding 1-D velocity models are shown by the same color. (b) A schematic (not to scale) diagram of the Mesopotamia crust stretched during the initial stage of rifting. Abbreviations are HZF, High Zagros Fault; MFF, Mountain Front Fault; Mp, Mesopotamian Plain; MZRF, Main Zagros Reverse Fault; ZFF, Zagros Foredeep Fault; EF, Euphrates Fault; KF, Kabir-kuh Fault. Geological information in (a) was adapted from 1, Motaghi, Shabanian, and Kalvandi (2017); 2, Berberian (1995); 3, Abdulnaby, Al-Mohmed, and Mahdi (2016); 4, Fouad (2015) and Sissakian et al. (2017); 5, Darweesh et al. (2017) and 6, Mohammed (2006) marked as numbers beside the related features.

5. Discussion

According to the available subsurface geological data (e.g., Al-Ameri, 2011; Aqrawi et al., 2010; Darweesh et al., 2017; Fadhel & Al-Rahim, 2019; Jassim & Goff, 2006; Mohammed, 2006), eastward thickening of the sedimentary cover in the Mesopotamian basin mainly corresponds to the eastward stepping of the Triassic and Middle to Late Jurassic normal faults, which have formed a depocenter at the eastern margin of the basin. The Abu Jir-Euphrates fault defines the southwest boundary against the Arabian stable platform (near the KAR2 where the thickness of the sediments changes sharply from 4 to 11 km; Figure 1), while the Makhul-Amara fault zone limits the northeast margin of the basin. Abdulnaby, Al-Mohmed, and Mahdi (2016)and Abdulnaby, Mahdi, et al. (2016) suggest a dip of 60° toward southwest for the southern sector of the Makhul-Amara fault zone (the so-called Badra-Amara fault). Darweesh et al. (2017) also proposes the same geometry. Combining the available geological and geophysical information, we suggest that the southwest migration of the Zagros deformation front (ZFF) superposed the eastern boundary of the graben through thrust faulting and folding in the sedimentary cover. Such kinds of shallow thrusts (e.g., ZFF) with opposite dip are commonly observed in sedimentary covers overlaying the inverted Paleozoic-Mesozoic rift systems (e.g., Lacombe et al., 2007; Madritsch et al., 2008). Interestingly, the crustal root in the east of the plain (Figure 9) corresponds to the Mesopotamian depocenter and is likely in relation with continuous loading of the stretched crust by Mesozoic to Quaternary deposits. This particular pattern is limited to the central domain of the Mesopotamian basin where NW-SE Triassic and Jurassic rift systems are well developed.

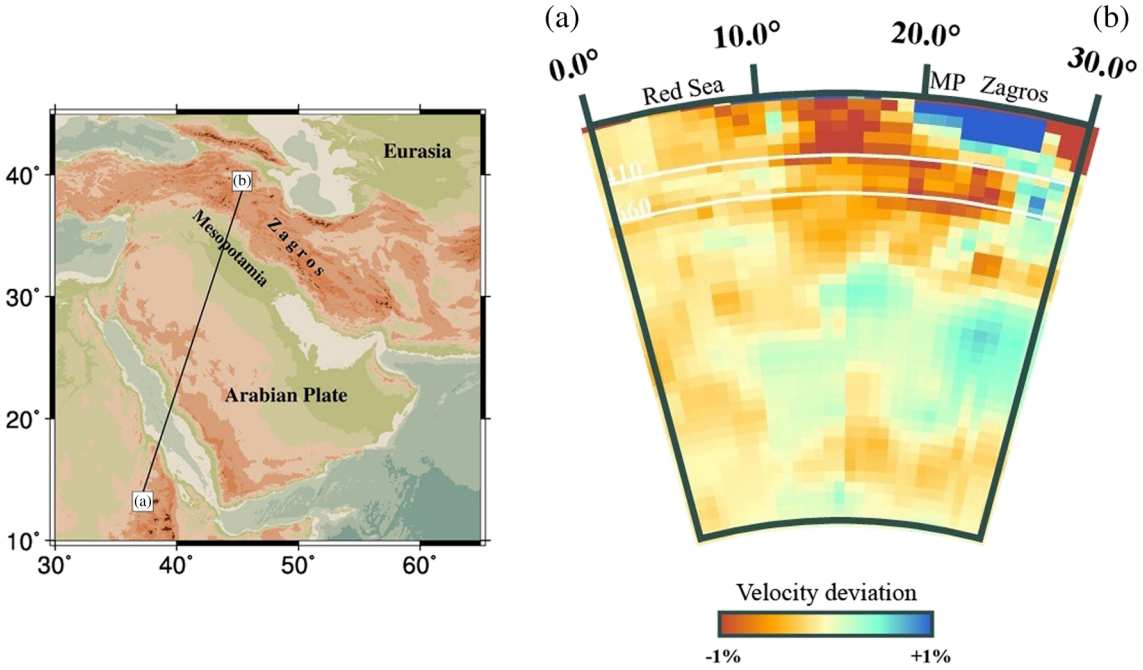

Figure 10. (left) A topography map of the Middle East (GTOPO30). Profile A-B shows the location of velocity cross section. (right) The velocity cross section along Profile A-B extracted from the world database of "Atlas of the Underworld" (http://www.atlas-of-the-underworld.org, Hall & Spakman, 2015). MP, Mesopotamia.

Transverse faults separate the central domain from the adjacent northwestern and southeastern domains (Figure 1; see section 1 for more details).

Local isostatic compensation implies that crustal roots usually accompany positive topography, while lowlands and active sedimentary basins have a thinner crust; in other words, surface topography is largely reflected in Moho topography. In the case of elastic response to loading (a normal elastic thickness), the region beneath the load subsides over a relatively wide area by displacing underneath flowing material and is complemented by the development of peripheral bulges (e.g., Kearey et al., 2009). As for the Mesopotamian Plain, surface and Moho topographies of the basin do not meet regular conditions for local isostatic or flexural bending compensation. For this reason, this research proposes that the successive rifting events and continuous subsidence of the basin between stepping normal faults (maximum sedimentary thickness of ~14 to 16 km in the depocenter; Figure 1) have generated considerable vertical loading over the depocenter leading to the generation of a crustal root (see the sketch in Figure 9). The middle to late Miocene rapid subsidence (Aqrawi & Badics, 2015), which is coeval with the late stage of the Zagros collision (e.g., Madanipour et al., 2013), enhanced downward thickening of the crust. This impeded important reverse fault movements due to tectonic inversion of the rift systems. Such a process requires a relatively weak lithospheric mantle (low effective elastic thickness) allowing the crust to locally sink under vertical loads and lateral contraction.

The 1-D velocity models (Figure 9) reveal a low-velocity uppermost mantle beneath the crustal root (Vs ~ 4.1 km/s) which is significantly slower than the lithospheric mantle beneath the Zagros Mountains (Vs ~ 4.8 km/s, Kaviani et al., 2007; Motaghi, Shabanian, & Kalvandi, 2017). This likely indicates a warmer and therefore weaker lithospheric mantle for the Mesopotamian Plain. The lithospheric mantle appears as weak as the lithosphere of Central Iran (Vs ~ 4.1–4.3 km/s, Motaghi et al., 2015 and Motaghi, Shabanian, & Kalvandi, 2017). However, the tectonomagmatic history undergone by Central Iran as the active continental margin for the past Neotethys subduction (e.g., Hassanzadeh & Wernicke, 2016) and affected by Paleogene to Oligocene magmatism (see Chiu et al., 2013, and references therein) is totally different from that of the Mesopotamian platform located behind the past Neotethys passive continental margin. The presence of this low-velocity zone is also consistent with regional-scale tomographic models of the mantle resolved for this area. This research investigated a regional-scale velocity cross section extracted from a global travel time tomography for the mantle (Figure 10). The seismic velocity model was retrieved from the

world database of "Atlas of the Underworld" (http://www.atlas-of-the-underworld.org) and was extracted from a global velocity model called "UU-P07" model (Amaru, 2007; Hall & Spakman, 2015). Figure 10 shows this cross section and its surficial expression. The model shows that the low-velocity anomaly beneath the Red Sea rift is asymmetrically extending toward the northern regions along the so-called tectonic equator (Panza et al., 2010). The northward flow of asthenospheric materials from the Red Sea rift was also proposed through investigating the Middle East mantle transition zone using a 3-D migration of *P* receiver functions (Kaviani et al., 2018) and a new regional travel time tomography for the Middle East (Wei et al., 2019). Kaviani et al. (2018) observed a thin mantle transition zone beneath the Red Sea extending northward beneath the Mesopotamian plain and concluded a hot material flow beneath the plain. This research suggests this hot flow as the source of the low velocity beneath the Mesopotamian Plain.

In summary, this research suggests that the crustal features observed beneath the Mesopotamian Plain (Figure 9) are a long-lasting effect of successive rifting of the Arabian platform in Triassic and Middle to Late Jurassic times enhanced by continuous sedimentary loading. The abnormal weak rheology of the Arabian upper mantle in this area has allowed local sinking of the crust and deepening of the Moho boundary due to vertical loading and lateral contraction. This scenario, which is different from the large-scale model for elastic flexural bending of the lithosphere under the collision loading, could explain sharp local variations in the structure of the crust. Taking such kinds of local structures into account would improve our large-scale models for mountain building, foreland basins evolution, and paleotectonic reconstructions. Figure 9 presents an interpretive summary of our observations through a conceptual tectonic cross section across the Mesopotamian Plain.

6. Conclusion

The *P* wave receiver functions for 12 seismic stations in the north, east, and central part of Iraq were calculated. The receiver functions were stacked and then jointly inverted with Rayleigh wave dispersion data. The models confirm the existence of an abnormal crustal root at the boundary between the Mesopotamian Plain and the Zagros front in SE Iraq, where the thickest sedimentary basin covers the crystalline basement. This was the result of successive rifting processes in the NE margin of the Arabian platform during Triassic and Middle to Late Jurassic. Sedimentary loading and continuous Mesozoic-Late Cenozoic subsidence have enhanced the sinking of the crust into the uppermost mantle. The produced seismic cross section reveals a significant low-velocity anomaly beneath the Mesopotamian Plain confirmed by available travel time global tomography studies. We believe that the weak rheology of the uppermost mantle allowed local sinking of the crust and deepening of the Moho boundary due to vertical loading and Late Cenozoic lateral contractions.

Data Availability Statement

Receiver Function data used in this study are made available online (at https://data.mendeley.com/datasets/8m9ydb3wds/1). Dispersion data are available through Kaviani et al. (2020). Continuous data from five of the used stations are broadcasted on real time to the Incorporated Research Institutions for Seismology (IRIS), and they are unrestricted for use by all interested researchers. Data from the other stations will be sequentially broadcasted to IRIS in the near future and will also be unrestricted for use by other researchers.

Acknowledgments

We warmly appreciate Dr. Laurent Jolivet (Editor), Dr. Douwe van Hinsbergen (Associate Editor), Dr. Jonathan Delph, and an anonymous reviewer for their helpful and constructive comments and suggestions. We are grateful to the Lawrence Livermore National Laboratory (LLNL) for supporting the installation of broadband seismic stations in Iraq. We also like to thank the University of Arkansas, Little Rock, for partially supporting this research. We thank Dr. Robert Herrmann (SLU) for the CPS software package.

References

Abdulnaby, W. (2013). Seismotectonics of the northeastern margin of the Arabian plate in Iraq (Doctoral dissertation, University of Arkansas at Little Rock).

Abdulnaby, W. (2019). Structural geology and neotectonics of Iraq, northwest Zagros. In *Developments in structural geology and tectonics* (Vol. 3, pp. 53–73). New York: Elsevier.

Abdulnaby, W., Al-Mohmed, R., & Mahdi, M. (2016). Seismicity and recent stress regime of Diyala City, Iraq–Iran border. *Modeling Earth Systems and Environment*, *2*(3), 142. https://doi.org/10.1007/s40808-016-0201-z

Abdulnaby, W., Mahdi, M., Al-Mohmed, R., & Mahdi, H. (2016). Seismotectonic of Badra-Amarah fault, Iraq-Iran border. *IOSR Journal of Applied Geology and Geophysics (IOSR-JAGG)*, *4*(3), 27–33.

Acton, C. E., Priestley, K., Mitra, S., & Gaur, V. K. (2011). Crustal structure of the Darjeeling–Sikkim Himalaya and southern Tibet. *Geophysical Journal International*, *184*(2), 829–852. https://doi.org/10.1111/j.1365-246X.2010.04868.x

Afsari, N., Sodoudi, F., Taghizadeh, F., & Reza, G. M. (2011). Crustal structure of northwest Zagros (Kermanshah) and Central Iran (Yazd and Isfahan) using teleseismic Ps converted phase. *Journal of Seismology*, *15*(2), 341–353. https://doi.org/10.1007/s10950-011-9227-x

Al-Ameri, T. K. (2011). Khasib and Tannuma oil sources, East Baghdad oil field, Iraq. *Marine and Petroleum Geology*, *28*(4), 880–894. https://doi.org/10.1016/j.marpetgeo.2010.06.003

Al-Damegh, K., Sandvol, E., & Barazangi, M. (2005). Crustal structure of the Arabian plate: New constraints from the analysis of teleseismic receiver functions. *Earth and Planetary Science Letters*, *231*(3–4), 177–196. https://doi.org/10.1016/j.epsl.2004.12.020

Al-Heety, E. A. M. (2002). Crustal structure of the northern Arabian platform inferred using spectral ratio method. *Journal of Geodynamics*, *34*(1), 63–75. https://doi.org/10.1016/S0264-3707(02)00017-0

Amaru, M. L. (2007). Global travel time tomography with 3-D reference models. *Geologica Ultraiectina*, *274*, 174.

Aqrawi, A. A., & Badics, B. (2015). Geochemical characterisation, volumetric assessment and shale-oil/gas potential of the middle Jurassic–lower cretaceous source rocks of NE Arabian plate. *GeoArabia*, *20*(3), 99–140.

Aqrawi, A. A., Goff, J. C., Horbury, A. D., & Saddoni, F. N. (2010). *The Petroleum Geology of Iraq*. Aberystwyth, UK: Scientific Press Ltd., Cambrian Printers.

Austermann, J., & Iaffaldano, G. (2013). The role of the Zagros orogeny in slowing down Arabia-Eurasia convergence since ~5 Ma. *Tectonics*, *32*, 351–363. https://doi.org/10.1002/tect.20027

Berberian, M. (1995). Master "blind" thrust faults hidden under the Zagros folds: Active basement tectonics and surface morphotectonics. *Tectonophysics*, *241*(3–4), 193–224. https://doi.org/10.1016/0040-1951(94)00185-C

Chiu, H. Y., Chung, S. L., Zarrinkoub, M. H., Mohammadi, S. S., Khatib, M. M., & Iizuka, Y. (2013). Zircon U–Pb age constraints from Iran on the magmatic evolution related to Neotethyan subduction and Zagros orogeny. *Lithos*, *162–163*, 70–87.

Cunningham, E., & Lekic, V. (2019). Constraining crustal structure in the presence of sediment: A multiple converted wave approach. *Geophysical Journal International*, *219*(1), 313–327. https://doi.org/10.1093/gji/ggz298

Darweesh, H. A., Obed, A. Z. M., & Albadran, B. N. (2017). Structural study of basins configuration in Mesopotamian area. *International Journal of Engineering and Applied Sciences*, *4*(9), 54–58.

Egan, S. S., Mosar, J., Brunet, M. F., & Kangarli, T. (2009). *Subsidence and uplift mechanisms within the South Caspian Basin: Insights from the onshore and offshore Azerbaijan region*, *Special Publications* (Vol. 312, pp. 219–240). London: Geological Society.

Fadhel, M. S., & Al-Rahim, A. M. (2019). A new tectono sedimentary framework of the Jurassic succession in the Merjan oil field, Central Iraq. *Journal of Petroleum Exploration and Production Technology*, *9*(4), 2591–2603. https://doi.org/10.1007/s13202-019-00750-1

Fouad, S. F. (2010a). Tectonic evolution of the Mesopotamia Foredeep in Iraq. *Iraqi Bulletin of Geology and Mining*, *6*(2), 41–53.

Fouad, S. F. (2010b). *Tectonic map of Iraq, Scale 1: 1000 000* (3rd ed.). Baghdad, Iraq: Geological Survey and Mineral Investigation (GEOSURV).

Fouad, S. F. (2015). Tectonic map of Iraq, scale 1: 1000 000, 2012. *Iraqi Bulletin of Geology and Mining*, *11*(1), 1–7.

Gök, R., Mahdi, H., Al-Shukri, H., & Rodgers, J. A. (2008). Crustal structure of Iraq from receiver functions and surface wave dispersion: Implications for understanding the deformation history of the Arabian-Eurasian collision. *Geophysical Journal International*, *172*(3), 1179–1187. https://doi.org/10.1111/j.1365-246X.2007.03670.x

Gök, R., Pasyanos, M., & Zor, E. (2007). Lithospheric structure of the continent–continent collision zone: Eastern Turkey. *Geophysical Journal International*, *169*(3), 1079–1088. https://doi.org/10.1111/j.1365-246X.2006.03288.x

Gritto, R. Sibol, M. S., Siegel, J. E., Ghalib, H. A., Chen, Y., Herrmann, R. B., et al. (2008). Crustal structure of North Iraq from receiver function analysis. Unpublished report from monitoring research review: Ground-based nuclear explosion monitoring technologies, sponsored by Air Force Research Laboratory, p. 8.

Hall, R., & Spakman, W. (2015). Mantle structure and tectonic history of SE Asia. *Tectonophysics*, *658*, 14–45. https://doi.org/10.1016/j.tecto.2015.07.003

Hassanzadeh, J., & Wernicke, B. P. (2016). The Neotethyan Sanandaj-Sirjan zone of Iran as an archetype for passive margin-arc transitions. *Tectonics*, *35*, 586–621. https://doi.org/10.1002/2015TC003926

Hatzfeld, D., & Molnar, P. (2010). Comparisons of the kinematics and deep structures of the Zagros and Himalaya and of the Iranian and Tibetan plateaus and geodynamic implications. *Reviews of Geophysics*, *48*, RG2005. https://doi.org/10.1029/2009RG000304

Herrmann, R. B. (2013). Computer programs in seismology: An evolving tool for instruction and research. *Seismological Research Letters*, *84*(6), 1081–1088. https://doi.org/10.1785/0220110096

Jaffar, H. M., & Abdulnaby, W. (2018). Stress regime of Rumania oilfield in southern Iraq from borehole breakouts. *IOSR Journal of Applied Geology and Geophysics*, *6*, 25–35.

Jassim, S. Z., & Goff, J. C. (2006). Geology of Iraq. Dolin, Prague and Moravian Museum, Brno, Czech Republic, p. 341.

Julia, J., Ammon, C. J., Herrmann, R. B., & Correig, A. M. (2000). Joint inversion of receiver functions and surface-wave dispersion observations. *Geophysical Journal International*, *143*, 99–112.

Kaviani, A., Paul, A., Bourova, E., Hatzfeld, D., Pedersen, H., & Mokhtari, M. (2007). A strong seismic velocity contrast in the shallow mantle across the Zagros collision zone (Iran). *Geophysical Journal International*, *171*(1), 399–410. https://doi.org/10.1111/j.1365-246X.2007.03535.x

Kaviani, A., Paul, A., Moradi, A., Mai, P. M., Pilia, S., Boschi, L., et al. (2020). Crustal and uppermost mantle shear-wave velocity structure beneath the Middle East from surface-wave tomography. *Geophysical Journal International*, *221*(2), 1349–1365. https://doi.org/10.1093/gji/ggaa075

Kaviani, A., Sandvol, E., Moradi, A., Rumpker, G., Tang, Z., & Mai, P. M. (2018). Mantle transition zone thickness beneath the Middle East: Evidence for segmented Tethyan slabs, delaminated lithosphere, and lower mantle upwelling. *Journal of Geophysical Research: Solid Earth*, *123*, 4886–4905. https://doi.org/10.1029/2018JB015627

Kearey, P., Klepeis, K. A., & Vine, F. J. (2009). *Global tectonics*. New York: John Wiley and Sons.

Kennett, B. L. N., & Engdahl, E. R. (1991). Travel times for global earthquake location and phase identification. *Geophysical Journal International*, *105*(2), 429–465. https://doi.org/10.1111/j.1365-246X.1991.tb06724.x

Khorrami, F., Vernant, P., Masson, F., Nilfouroushan, F., Mousavi, Z., Nankali, H., et al. (2019). An up-to-date crustal deformation map of Iran using integrated campaign-mode and permanent GPS velocities. *Geophysical Journal International*, *217*(2), 832–843. https://doi.org/10.1093/gji/ggz045

Lacombe, O., Amrouch, K., Mouthereau, F., & Dissez, L. (2007). Calcite twinning constraints on late Neogene stress patterns and deformation mechanisms in the active Zagros collision belt. *Geology*, *35*(3), 263–266. https://doi.org/10.1130/G23173A.1

Ligorria, J. P., & Ammon, C. J. (1999). Iterative deconvolution and receiver-function estimation. *Bulletin of the Seismological Society of America*, *89*(5), 1395–1400.

Madanipour, S., Ehlers, T. A., Yassaghi, A., Rezaeian, M., Enkelmann, E., & Bahroudi, A. (2013). Synchronous deformation on the orogenic plateau margins, insights from the Arabia-Eurasia collision. *Tectonophysics*, *608*, 440–451. https://doi.org/10.1016/j.tecto.2013.09.003

Madritsch, H., Schmid, S. M., & Fabbri, O. (2008). Interactions between thin-and thick-skinned tectonics at the northwestern front of the Jura fold-and-thrust belt (eastern France). *Tectonics*, *27*, TC5005. https://doi.org/10.1029/2008TC002282
McQuarrie, N., & van Hinsbergen, D. J. (2013). Retrodeforming the Arabia-Eurasia collision zone: Age of collision versus magnitude of continental subduction. *Geology*, *41*(3), 315–318. https://doi.org/10.1130/G33591.1
Mellors, R., Gök, R., Pasyanos, M., Skobeltsyn, G., Teoman, U., Godoladze, T., & Sandvol, E. (2008). High-resolution seismic velocity and attenuation models of the Caucasus-Caspian Region, LLNL-Proc-405214.
Mohammed, S. A. (2006). Megaseismic section across the northeastern slope of the Arabian plate, Iraq. *GeoArabia*, *11*(4), 77–90.
Motaghi, K., Shabanian, E., & Kalvandi, F. (2017). Underplating along the northern portion of the Zagros suture zone, Iran. *Geophysical Journal International*, *210*(1), 375–389. https://doi.org/10.1093/gji/ggx168
Motaghi, K., Shabanian, E., Tatar, M., Cuffaro, M., & Doglioni, C. (2017). The south Zagros suture zone in teleseismic images. *Tectonophysics*, *694*, 292–301. https://doi.org/10.1016/j.tecto.2016.11.012
Motaghi, K., Tatar, M., Priestley, K., Romanelli, F., Doglioni, C., & Panza, G. F. (2015). The deep structure of the Iranian plateau. *Gondwana Research*, *28*(1), 407–418. https://doi.org/10.1016/j.gr.2014.04.009
Numan, N. M. S. (1997). A plate tectonic scenario for the phanerozoic succession in Iraq. *Journal of the Geological Society of Iraq*, *30*(2), 85–110.
Numan, N. M. S. (2000). Major cretaceous tectonic events in Iraq. *Rafidain Journal of Science*, *11*(3), 32–52.
Panza, G., Doglioni, C., & Levshin, A. (2010). Asymmetric ocean basins. *Geology*, *38*(1), 59–62. https://doi.org/10.1130/G30570.1
Pasyanos, M. E., Tkalcic, H., Gök, R., Al-Enezi, A., & Rodgers, A. (2007). Seismic structure of Kuwait. *Geophysical Journal International*, *170*(1), 299–312. https://doi.org/10.1111/j.1365-246X.2007.03398.x
Paul, A., Kaviani, A., Hatzfeld, D., Tatar, M., & Pequegnat, C. (2010). Seismic imaging of the lithospheric structure of the Zagros mountain belt (Iran). In P. Leturmy & C. Robin (Eds.), *Tectonic and Stratigraphic Evolution of Zagros and Makran During the Meso-Cenozoic*, *Special Publications* (Vol. 330, pp. 5–18). London: Geological Society.
Paul, A., Kaviani, A., Hatzfeld, D., Vergne, J., & Mokhtari, M. (2006). Seismological evidence for crustal-scale thrusting in the Zagros mountain belt (Iran). *Geophysical Journal International*, *166*(1), 227–237. https://doi.org/10.1111/j.1365-246X.2006.02920.x
Pirouz, M., Avouac, J. P., Gualandi, A., Hassanzadeh, J., & Sternai, P. (2017). Flexural bending of the Zagros foreland basin. *Geophysical Journal International*, *210*(3), 1659–1680. https://doi.org/10.1093/gji/ggx252
Pirouz, M., Avouac, J. P., Hassanzadeh, J., Kirschvink, J. L., & Bahroudi, A. (2017). Early Neogene foreland of the Zagros, implications for the initial closure of the neo-Tethys and kinematics of crustal shortening. *Earth and Planetary Science Letters*, *477*, 168–182. https://doi.org/10.1016/j.epsl.2017.07.046
Priestley, K., McKenzie, D., Barron, J., Tatar, M., & Debayle, E. (2012). The Zagros core: Deformation of the continental lithospheric mantle. *Geochemistry, Geophysics, Geosystems*, *13*, Q11014. https://doi.org/10.1029/2012GC004435
Rahimi, H., Hamzehloo, H., Vaccari, F., & Panza, G. F. (2014). Shear-wave velocity tomography of the lithosphere–asthenosphere system beneath the Iranian plateau. *Bulletin of the Seismological Society of America*, *104*(6), 2782–2798. https://doi.org/10.1785/0120130319
Rahmani, M., Motaghi, K., Ghods, A., Sobouti, F., Talebian, M., Ai, Y., & Chen, L. (2019). Deep velocity image of the north Zagros collision zone (Iran) from regional and teleseismic tomography. *Geophysical Journal International*, *219*(3), 1729–1740. https://doi.org/10.1093/gji/ggz393
Rastgoo, M., Rahimi, H., Motaghi, K., Shabanian, E., Romanelli, F., & Panza, G. F. (2018). Deep structure of the Alborz Mountains by joint inversion of *P* receiver functions and dispersion curves. *Physics of the Earth and Planetary Interiors*, *277*, 70–80. https://doi.org/10.1016/j.pepi.2018.01.011
Schulte-Pelkum, V., & Mahan, K. H. (2014). A method for mapping crustal deformation and anisotropy with receiver functions and first results from USArray. *Earth and Planetary Science Letters*, *402*, 221–233. https://doi.org/10.1016/j.epsl.2014.01.050
Sissakian, V., Al-Ansari, N., & Knutsson, S. (2014). Origin of some transversal linear features of NE-SW trend in Iraq, and their geological characters. *Natural Science*, *06*(12), 996–1011. https://doi.org/10.4236/ns.2014.612091
Sissakian, V. K., Al-Ansari, N., Adamo, N., Laue, J., & Knutsson, S. (2018). Geology of the Euphrates River with emphasize on the Iraqi part. *Journal of Earth Sciences and Geotechnical Engineering*, *8*(3), 167–185.
Sissakian, V. K., Shihab, A. T., Al-Ansari, N., & Knutsson, S. (2017). New tectonic finding and its implications on locating oilfields in parts of the Gulf Region. *Journal of Earth Sciences and Geotechnical Engineering*, *7*(3), 51–75.
Snyder, D. B., & Barazangi, M. (1986). Deep crustal structure and flexure of the Arabian plate beneath the Zagros collisional mountain belt as inferred from gravity observations. *Tectonics*, *5*(3), 361–373. https://doi.org/10.1029/TC005i003p00361
Tatar, M., & Nasrabadi, A. (2013). Crustal thickness variations in the Zagros continental collision zone (Iran) from joint inversion of receiver functions and surface wave dispersion. *Journal of Seismology*, *17*(4), 1321–1337. https://doi.org/10.1007/s10950-013-9394-z
Teknik, V., Ghods, A., Thybo, H., & Artemieva, I. M. (2019). Crustal density structure of the northwestern Iranian plateau. *Canadian Journal of Earth Sciences*, *56*(12), 1347–1365. https://doi.org/10.1139/cjes-2018-0232
Wei, W., Zhao, D., Wei, F., Bai, X., & Xu, J. (2019). Mantle dynamics of the eastern Mediterranean and Middle East: Constraints from *P*-wave anisotropic tomography. *Geochemistry, Geophysics, Geosystems*, *20*, 4505–4530. https://doi.org/10.1029/2019GC008512
Zhu, L. P., & Kanamori, H. (2000). Moho depth variation in southern California from teleseismic receiver functions. *Journal of Geophysical Research*, *105*(B2), 2969–2980. https://doi.org/10.1029/1999JB900322